Simultaneous Total Variation Image Inpainting and Blind Deconvolution *

Tony F. Chan† Andy M. Yip† Frederick E. Park†

July 7, 2004

Abstract

We propose a total variation based model for simultaneous image inpainting and blind deconvolution. We demonstrate that the tasks are inherently coupled together and that solving them individually will lead to poor results. The main advantages of our model are that (i) boundary conditions for deconvolution required near the interface between observed and occluded regions are naturally generated through inpainting; (ii) inpainting results are enhanced through deconvolution (as opposed to inpainting blurry images). As a result, ringing effects due to imposing improper boundary conditions and errors due to imperfection of inpainting blurry images are reduced. Moreover, our model can also be used to generate boundary conditions for regular deconvolution problems that yields better results than previous methods.

1 Introduction

Image restoration problems such as inpainting and deblurring have always been important image processing tasks with many real world applications. The blurring of images often times occurs from the motion of objects, calibration errors with imaging devices, or even from unfocused cameras. Mathematically, we state the forward model of the blurring process as:

$$f = k * u + \eta. \tag{1}$$

Here, f is the observed image defined on a domain Ω (usually a rectangle in $\mathbb{R}^2$), u the true image also defined on Ω, k the point spread function (PSF), η the additive noise, and $*$ the convolution operator. Thus, the blind deconvolution task amounts to recovering u and k given only the observed image f. There are many methods for simultaneous recovery of the deblurred image u and the PSF k in the above model (1) which may include inverse filtering, statistical, and Tikhonov regularization methods. For inverse filtering methods, we refer the read to [14, 23, 24]. For statistical methods, see [18, 16, 12, 25]. For Tikhonov regularization methods, in particular for H^1 regularization we direct the reader to [31] and for total variation (TV) regularization to [9, 17, 28, 29, 32]. A survey on blind image deconvolution may also be found in [13].

Often times images may also have regions with missing data. Examples may include scratches on film frames, scratches on images, the occlusion of objects in an image, or even from irregularities in the

*This work was partially supported by grants from the NSF under contract DMS-9973341, the ONR under contract N00014-03-1-0888 and the NIH under contract MH65166.

†Department of Mathematics, University of California, 405 Hilgard Avenue, Los Angeles, CA 90095-1555. Email: {chan,mhyip,fpark}@math.ucla.edu

imaging device itself (e.g. scratched lenses). To remedy these problems, we consider image inpainting which is the filling in of missing data based on known information. One of the earliest works on digital inpainting is the work by Bertalmio et al in [2] where the authors' motivation comes from the professional artists who restore damaged ancient paintings by hand. There are many inpainting models and we refer the reader to [8, 1, 3, 6, 7, 19] for some recent works and references therein.

The problem we address and wish to solve in this paper is the restoration of blurred images with occluded or missing regions arising from multiple degradation processes. More precisely, the degradation model is given by:

$$\begin{aligned} f &= k * u + \eta \qquad \text{on } \Omega \\ f\,|_{D_i} &\qquad \text{unknown.} \end{aligned} \tag{2}$$

Here, $D_i \subset \Omega$ is the given missing region. This problem cannot be properly solved separately (e.g. deblurring then inpainting or vice versa) because the two restoration tasks are inherently coupled (see §2.3–2.4). Moreover, errors from one step cannot be easily corrected in the subsequent steps and may possibly be amplified, yielding severe ringing effects [15].

The proposed model is a simultaneous inpainting and deblurring model and will be shown to overcome the above mentioned difficulties. Moreover, this model will prove to be further advantageous as it is easier to implement and more efficient than solving the problem by applying two separate methods. This will prove to be a novel idea of combining the two inpainting and deblurring processes into one simultaneous method and to the best of the authors' knowledge, has not been addressed before.

The rest of the paper is organized as follows. In §2, we first introduce the TV blind image deconvolution and inpainting models and then present some of their potential drawbacks for recovering blurred and occluded images. The joint TV deblurring and inpainting model is presented in §3. A novel use for automatic boundary condition generation for deblurring via inpainting is introduced in the next section, §4. In §5, a description of the numerical implementations is given. In §6, numerical simulations are performed on both synthetic and real world images. Finally, a short conclusion is given in §7.

2 TV Blind Image Deconvolution and Inpainting Models

2.1 TV Blind Image Deconvolution

There are many methods for recovering the deblurred image u in the forward model (1). One of the more popular blind deconvolution models is based on the joint minimization of the following energy:

$$E_{\text{decon}}(u,k) = \frac{\alpha}{2}\int_\Omega (k*u-f)^2 dx + R_1(u) + \beta R_2(k).$$

In [31], You and Kaveh choose $R_1(u) = \int_\Omega |\nabla u|^2 dx$ and $R_2(k) = \int_\Omega |\nabla k|^2 dx$ as the regularization functionals. One potential drawback of using such a regularization is that the minimization of the H^1-norm tends to smear edges in both the recovered image and PSF. In view of this, Chan and Wong, in [9], utilize total variation (TV) regularization $R_1(u) = \int_\Omega |\nabla u| dx$ and $R_2(k) = \int_\Omega |\nabla k| dx$ which favors the preservation of edge information (discontinuities) [26]. Hence, restored image and PSF features tend to be sharper with less diffusion. More precisely, the Chan-Wong model is given by:

$$E_{\text{decon}}(u,k) = \frac{\alpha}{2}\int_\Omega (k*u-f)^2 dx + \int_\Omega |\nabla u| dx + \beta\int_\Omega |\nabla k| dx \tag{3}$$

which chooses the balance between a good fit to the original data f and regularization. The parameters α and β control the amount of regularization which is given by the TV norm in both k and u.

2.2 TV Image Inpainting

In this paper we will focus on the TV inpainting model [7] which is variational and fits well with the TV blind deconvolution model (3). It has several benefits including an easy implementation, a tendency towards preserving edges, and a robustness to noise. Moreover, the TV model also serves as a basic building block for some other higher order inpainting models.

For inpainting problems, the TV inpainting model seeks a balance between a fitting term and a fidelity term. The fitting term is only applied on the non-occluded or non-missing regions while the fidelity term is applied to the whole image domain. Precisely,

$$E_{\text{inpaint}}(u) \quad = \quad \frac{\alpha}{2}\int_{\Omega\setminus D_i}(u-f)^2dx + \int_{D_i}|\nabla u|dx. \tag{4}$$

Here, Ω is the entire image domain and D_i is the inpainting domain (occluded or missing image region). In this paper, the TV-norm serves a dual purpose as both a regularizer and inpainting method for the proposed simultaneous blind deconvolution and inpainting model.

2.3 Difficulties of Deconvolving Occluded Images

Given a blurred image with missing or occluded regions, the deconvolution problem (even when the PSF is known) becomes difficult as there are some complications in addition to the well-known ill-conditioning. The foremost complication is finding the appropriate boundary conditions for the missing regions. Due to the averaging over the support of the convolution kernel, the problem requires image information that extends beyond the boundary of the observed regions (c.f. Fig. 1(c)). This proves particularly troublesome in the inpainting domain (missing region) since the boundary conditions may not be well defined. For example, if we consider an inpainting domain under either homogeneous Neumann (c.f. Fig. 1(d)) or Dirichlet (c.f. Fig. 1(e)) boundary conditions, the extended information into the inpainting domain may not be the correct extension of the missing data. This incorrect extension of the missing data at the boundary of either the image or inpainting domain is then averaged with the available image information over the support of the PSF yielding an incorrect approximation to the convolution product $k * u$ seen in (3). Thus, errors propagate into the non-occluded parts of the image itself causing ringing effects during the deconvolution process, regardless of the particular deconvolution method used. For more examples of the ringing phenomenon due to boundary conditions we refer the reader to [22, 27, 21].

We will show that by coupling the deconvolution and inpainting problems, it is possible to construct boundary conditions based on smooth extension of the level sets. This leads to a more natural boundary conditions (c.f. Fig. 1(f)), and hence, less ringing effects.

2.4 Problems Associated to the Inpainting of Blurred Images

A key difficulty that arises from the inpainting of blurred images is that it leads to ambiguities in the reconstruction of the deblurred images. We illustrate this situation in Fig. 2. In the figure, we show two sets of original signals and PSFs whose resulting blurred and occluded signals in Fig. 2 (d) and (h) are identical. If one applies an inpainting algorithm on the two signals, then in both cases inpainting favors a recovery similar to the one in Fig. 2 (g). In the case of TV inpainting, we recover Fig. 2 (g) exactly. Thus, in the blind deconvolution of the inpainted blurred signal there is a bias towards the recovery of Fig. 2 (e) and (f) whereas the true signal and PSF may be Fig. 2 (a) and (b). As a result, due to the local process of inpainting, there is the possibility that the PSF corresponding to the inpainting region does not match that of the observed image region. This suggests that a good model

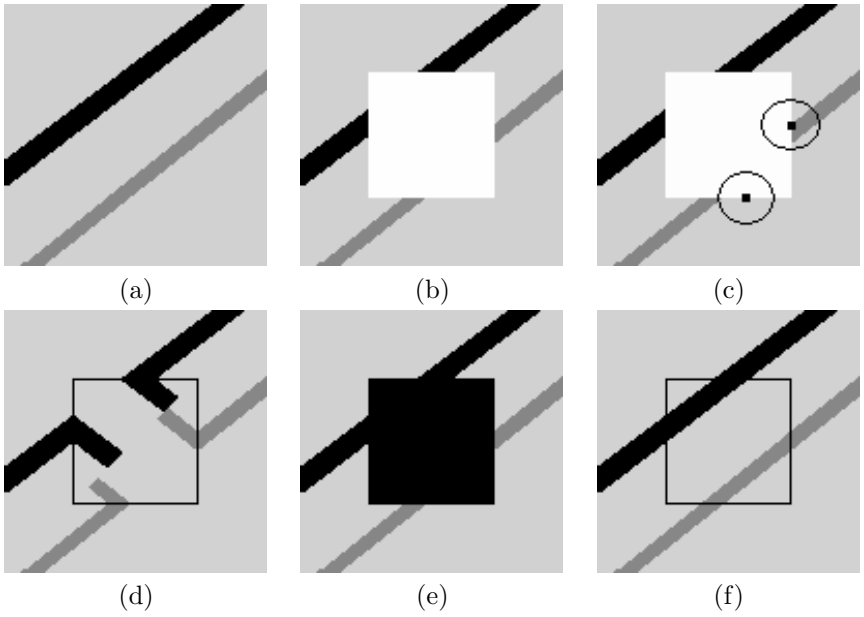

Figure 1: Boundary conditions (B.C.). (a) Original clean image. (b) Original image with missing region. (c) Original image with missing region with PSF support of two sample pixels shown as the dark circles. The circles show some of the extended domain of dependency for the convolution operator as seen in (2). (d) Homogeneous Neumann (reflection) B.C. (e) Homogeneous Dirichlet (Zero) B.C. (f) A B.C. based on objects' connectivity. The black box outline in (d) and (f) marks the boundary of inpainting domain in (b).

for this problem should be able to incorporate information away from the inpainting region to ensure that the correct PSF is chosen. If the true signal and PSF are Fig. 2 (a) and (b) then the model should be able to recover Fig. 2 (c) as the inpainted result (for $k * u$). Likewise, for the true signal and PSF Fig. 2 (e) and (f), the model should be able to recover Fig. 2 (g) as the inpainted result (for $k * u$). The model we develop in §3 will accomplish this.

2.5 Benefits of Simultaneous Inpainting and Deconvolution

To alleviate the above mentioned difficulties associated with solving the two methods separately (e.g. deblur then inpaint or vice versa), we propose a simultaneous inpainting and blind deconvolution method of restoring blurred images with occluded or missing regions.

By simultaneously combining inpainting and deconvolution, we may overcome the difficulty of imposing appropriate boundary conditions for the inpainting domain in the case of deblurring images with occluded or missing regions. Hence, the ringing effects are greatly reduced compared to the reconstruction using separate methods, c.f. Fig. 5 and 6. Moreover, the problem of ambiguities when inpainting blurry images is also resolved by incorporating global information about the PSF from both the inpainting and observed image regions.

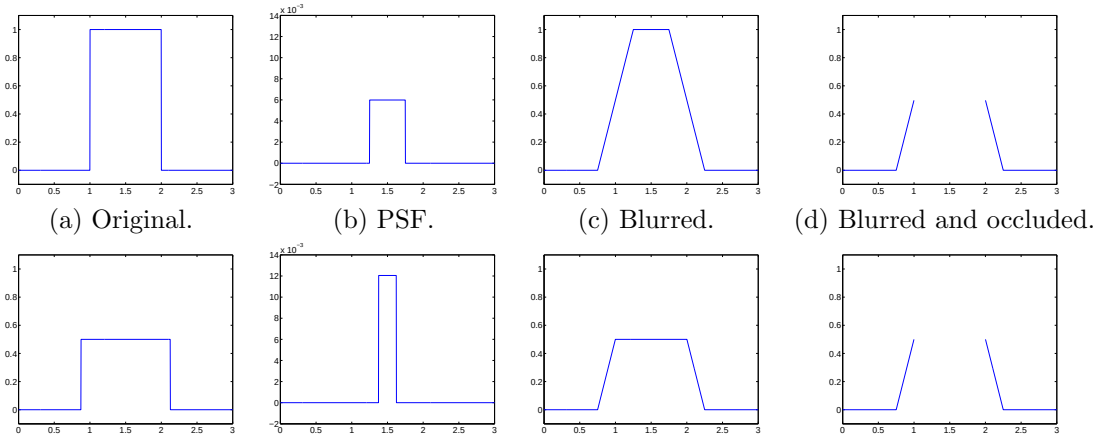

(a) Original. (b) PSF. (c) Blurred. (d) Blurred and occluded.

(e) Original. (f) PSF. (g) Blurred. (h) Blurred and occluded.

Figure 2: Ambiguity of blurry signals with a missing region. In (d) and (h), the missing region is the interval $[1, 2]$.

3 A Joint Deblurring and Inpainting Model

In this section, we describe our model for simultaneous image inpainting and blind deconvolution. We first fix some notations.

- D_o — the region where the image is observed
- D_i — the region to be inpainted (c.f. Fig. 3(a))
- D_k — the domain where the PSF is defined

Our model is based on the minimization of the following energy which is a natural generalization of the TV blind deconvolution and the TV inpainting models in (3) and (4):

$$\min_{u,k} E(u,k) \quad \equiv \quad \min_{u,k} \frac{\alpha}{2} \int_{D_o} (k * u - f)^2 dx + \int_{D_o \cup D_i} |\nabla u| dx + \beta \int_{D_k} |\nabla k| dx. \tag{5}$$

Here, α, $\beta > 0$ are regularization parameters that play the same role as the parameters in models (3) and (4). Indeed, α depends on the noise level $\|\eta\|$, c.f. (2). In general, as the noise level increases, the value of α should be decreased. If the noise level is known, then one may use the Morozov Principle [20] to obtain a good choice of α. If the noise level is unknown, then one may use methods such as L-curve [11] or generalized cross-validation [25] instead. The parameter β controls the spread of the recovered PSF. When β increases, the spread of the recovered PSF increases. For example, in the particular case where k is an out-of-focus blur [15], the focal length of the recovered PSF increases with β.

Such an energy may be written as the sum of a "deconvolution energy" $E_{\text{decon}}(u,k)$ and an "inpainting energy" $E_{\text{inpaint}}(u)$:

$$\begin{aligned} E(u,k) &= E_{\text{decon}}(u,k) + E_{\text{inpaint}}(u) \\ E_{\text{decon}}(u,k) &= \frac{\alpha}{2} \int_{D_o} (k * u - f)^2 dx + \int_{D_o} |\nabla u| dx + \beta \int_{D_k} |\nabla k| dx \end{aligned}$$

$$E_{\text{inpaint}}(u) \quad = \quad \int_{D_i} |\nabla u| dx.$$

Clearly, $E_{\text{decon}}(u,k)$ and $E_{\text{inpaint}}(u)$ have the same form as (3) and (4) respectively. Thus, roughly speaking, the model performs blind deconvolution inside D_o where the data are observed and performs inpainting inside D_i where the data are missing. The question is how the model behaves exactly around the interface of D_o and D_i where the problems of deconvolution and inpainting are coupled together.

To explain how the model works around the interface, let us first decompose the image into three regions $\{D_o, D_i \setminus I, I\}$ according to how the convolution product $k * u$ appearing in the first term of (5) depends on the value of u in $D_o \cup D_i$. In fact, the convolution $k * u$ at x_0 depends on the support of the kernel $k(x_0 - y)$ centered at x_0. Thus, we define the domain of dependence of $k * u$ at x_0 by

$$\{y \in D_o \cup D_i \mid k(x_0 - y) > 0\}.$$

In Fig. 3(b), we illustrate some sample points in D_i at which their domain of dependence (shown as dotted circles) intersects with both D_o and D_i (assuming the support of k is a circle centered at 0). The collection of such points in D_i is denoted by I, see Fig. 3(c) where the domain $D_o \cup D_i$ is then decomposed into three components $\{D_o, D_i \setminus I, I\}$. Intuitively, the set I is a ring around the interface of D_o and D_i.

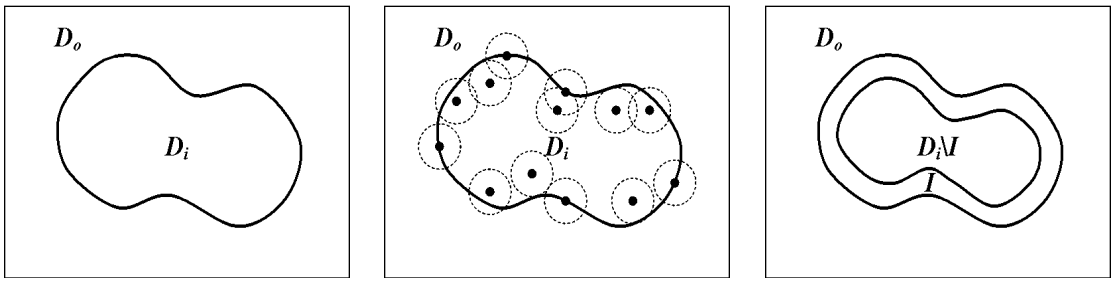

(a) (b) (c)

Figure 3: (a) Observed region D_o and inpainting region D_i. (b) Some sample pixels (black dots) in D_i whose domain of dependence of $k * u(x)$ (dotted circles) crosses both D_o and D_i. (c) Decomposition of the image into three regions $\{D_o, D_i \setminus I, I\}$.

The energies $E_{\text{decon}}(u,k)$ and $E_{\text{inpaint}}(u)$ are coupled together in the component region I because the convolution $k * u$ evaluated in D_o depends on the value of u in D_o as well as in I. In particular, the deconvolution problem in D_o is ill-posed (no unique solution) unless the value of u in I has been specified. However, specifying $u(I)$ using an arbitrary value or by techniques such as reflection may result in ringing effects when the imputed (filled-in) value differs considerably from the underlying true value. A reasonable way to impute $u(I)$ is to extrapolate $u(D_o)$ into I in a smooth and edge-preserving way which can be accomplished by TV regularization on u, c.f. (5). We may now understand the model (5) as performing the following tasks simultaneously:

- Perform blind deconvolution in D_o;
- Fill-in the value $u(I)$ such that the transition of the (deblurred) image between the regions D_o and I is smooth and edge-preserving;
- Fill-in the value $u(D_i \setminus I)$ such that the transition of the image between the regions I and $D_i \setminus I$ is smooth and edge-preserving.

4 Automatic Boundary Condition Generation via Inpainting

Besides deblurring occluded images, the interplay between deconvolution and inpainting also gives rise to another useful application in image reconstruction — generation of boundary conditions.

In image restoration problems such as deblurring and super-resolution reconstruction [22], it is necessary to impose some boundary conditions (image intensity value right outside the scene) to make the problem solvable because the convolution $k * u$ in (3) evaluated near the boundary of an image (c.f. Fig. 4(a)) depends on the image intensity outside the scene which is unknown. Improper assumptions made on the boundary conditions may deteriorate the quality of the reconstructed images, e.g. ringing effects and loss of contrast [22]. Over the years, there have been a number of research articles addressing the problem of imposing proper boundary conditions for image restoration. The main considerations in these papers have been the quality of the restored images and computational efficiency (some of these boundary conditions allow fast transform based deblurring). The commonly used boundary conditions are homogenous Dirichlet/zero (see Fig. 4(b)) and periodic [15] (see Fig. 4(c)). Neumann [21] (see Fig. 4(d)) and anti-reflective [27] (not shown because it contains negative values) boundary conditions are more recent ones that have been shown to outperform the former two.

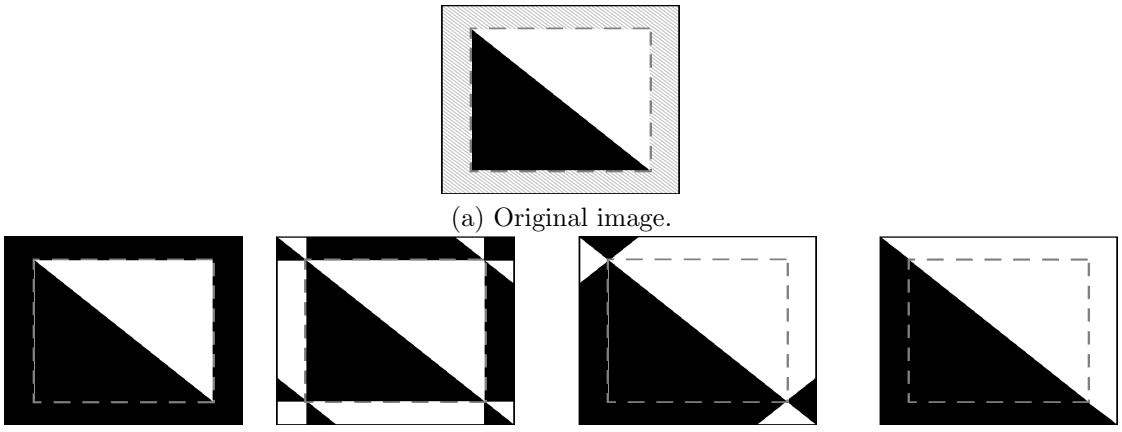

(a) Original image.

(b) Dirichlet (zero). (c) Periodic. (d) Neumann (reflection). (e) Inpainting.

Figure 4: Different types of boundary conditions (B.C.) In (a), the original image is the two triangles with the boundary depicted as a shaded ring. (b) through (e) Various B.C.

While the aforementioned boundary conditions are easy to construct, they make no attempt to fill-in the boundary based on the geometry of the isophotes. As a result, the assumed boundary values may seem to be very unnatural, see Fig. 4(b)–(d). However, making use of geometric information becomes straightforward in the framework of inpainting. If we treat the boundary, which depends on the size of support of the PSF, as an inpainting region D_i, then one may simply employ the model (5) to perform deconvolution and automatically generate a very natural boundary condition, see Fig. 4(e). We call such boundary conditions *inpainting boundary conditions*. Of course, the exact value of the inpainting boundary condition may depend on the particular inpainting method used. But most inpainting methods (including the TV one we use) are geometric based and lead to more natural imputed values. However, in the case of linear regularization operators such as the H^1-norm, other boundary conditions such as the Neumann and anti-reflective ones allow the use of fast Discrete Cosine/Sine Transforms to solve the deconvolution problem [27, 22, 21, 15].

5 Numerical Implementations

The minimization of the energy in (5) is carried out by alternating minimization [9], i.e., given an initial guess u^0, we alternate between the following two steps until the iterates u^n and k^n become stable:

1. Solve k^{n+1} by $\min_k E(u^n, k)$.
2. Solve u^{n+1} by $\min_u E(u, k^{n+1})$.

The Euler-Lagrange equations for the above two minimization problems are

$$\begin{aligned} \alpha u^n(-x) * (u^n * k - f) - \beta \nabla \cdot \frac{\nabla k}{|\nabla k|} &= 0 \qquad \text{in } D_k \\ \frac{\partial k}{\partial n} &= 0 \qquad \text{on } \partial D_k \end{aligned}$$

and

$$\begin{aligned} \alpha \chi_{D_o} k^{n+1}(-x) * (k^{n+1} * u - f) - \nabla \cdot \frac{\nabla u}{|\nabla u|} &= 0 \qquad \text{in } D_o \cup D_i \\ \frac{\partial u}{\partial n} &= 0 \qquad \text{on } \partial(D_o \cup D_i) \end{aligned}$$

respectively. Here, χ_{D_0} is 1 in D_o and 0 otherwise.

One simple method to solve the above equations is gradient descent which amounts to finding the steady states of the following equations

$$\begin{aligned} \frac{\partial k}{\partial t} &= -\alpha u^n(-x) * (u^n * k - f) + \beta \nabla \cdot \frac{\nabla k}{|\nabla k|} \qquad \text{in } D_k \\ \frac{\partial k}{\partial n} &= 0 \qquad \text{on } \partial D_k \end{aligned} \tag{6}$$

and

$$\begin{aligned} \frac{\partial u}{\partial t} &= -\alpha \chi_{D_o} k^{n+1}(-x) * (k^{n+1} * u - f) + \nabla \cdot \frac{\nabla u}{|\nabla u|} \qquad \text{in } D_o \cup D_i \\ \frac{\partial u}{\partial n} &= 0 \qquad \text{on } \partial(D_o \cup D_i). \end{aligned} \tag{7}$$

Given an observed image $\{f_{ij}\}$ for $i = 1, \ldots, m_1$ and $j = 1, \ldots, m_2$, we would like to solve a discretized version of (6) and (7) alternatively to obtain the recovered image $\{u_{ij}\}$ and the PSF $\{k_{ij}\}$. Let $\mathbf{f}$, $\mathbf{u}$ and $\mathbf{k}$ be $(m_1 m_2)$-by-1 vectors containing the entries $\{f_{ij}\}$, $\{u_{ij}\}$ and $\{k_{ij}\}$ in column scan ordering respectively. Given $\mathbf{u}^n$, we may obtain $\mathbf{k}^{n+1}$ by iterating on $l = 1, 2, \ldots$ the following forward Euler finite difference discretization of (6)

$$\mathbf{k}_{l+1}^{n+1} = \mathbf{k}_l^{n+1} + \Delta t \left[-\alpha A_{\mathbf{u}^n}^T (A_{\mathbf{u}^n} \mathbf{k}_l^{n+1} - \mathbf{f}) - \beta L_{\mathbf{k}_l^{n+1}} \mathbf{k}_l^{n+1} \right]. \tag{8}$$

Similarly, given $\mathbf{k}^{n+1}$, we may obtain $\mathbf{u}^{n+1}$ by iterating on $l = 1, 2, \ldots$ the following forward Euler finite difference discretization of (7)

$$\mathbf{u}_{l+1}^{n+1} = \mathbf{u}_l^{n+1} + \Delta t \left[-\alpha \Lambda A_{\mathbf{k}^{n+1}}^T (A_{\mathbf{k}^{n+1}} \mathbf{u}_l^{n+1} - \mathbf{f}) - L_{\mathbf{u}_l^{n+1}} \mathbf{u}_l^{n+1} \right]. \tag{9}$$

Here,

- $\Delta t > 0$ is the time step parameter;
- $\Lambda = \text{diag}(\lambda_{1,1}, \ldots, \lambda_{m_1,1}, \lambda_{1,2}, \ldots, \lambda_{m_1,m_2})$ is an $(m_1 m_2)$-by-$(m_1 m_2)$ diagonal matrix with $\lambda_{i,j} = 1$ if $u_{ij} \in D_o$ and 0 otherwise;
- $A_{\mathbf{v}}$ is a matrix representation of the blur operator with PSF v;
- $L_{\mathbf{v}}$ is an $(m_1 m_2)$-by-$(m_1 m_2)$ matrix representation of the differential operator $-\nabla \cdot (\nabla / |\nabla v|)$.

We refer the readers to [4] for details on the construction of the matrices $A_{\mathbf{v}}$ and $L_{\mathbf{v}}$.

We remark that the above forward Euler schemes (8) and (9) are implemented for simplicity; other finite difference schemes may be used as well. In addition, the Euler-Lagrange equations (which are static problems) may be solved directly without the introduction of artificial time variables. For example, one may easily implement the lagged diffusivity fixed point iteration method [30] and solve the arising linear systems via the preconditioned conjugate gradient method as outlined in [9]. Indeed, the schemes in (8) and (9) have already been expressed in matrix form which are very similar to the ones in [9]. Thus, it is very easy to adapt the fast methods in [9] to solve the current problem. The major difference is that if we employ the fixed point iteration method or some implicit finite difference schemes, then we may encounter the problem of solving (non-symmetric) linear systems of the form $(L + \alpha \Lambda A^T A)\mathbf{x} = \mathbf{b}$ which is slightly different from the kind of linear systems $(L + \alpha A^T A)\mathbf{x} = \mathbf{b}$ encountered in [9] and may require new techniques to optimize the performance when solving them.

6 Simulation Results

In this section, we use numerical simulations to illustrate the benefits of using the proposed simultaneous model. We assume a parametric form of the PSF so that the recovery of k becomes the estimation of the associated parameters. A non-parametric form of the PSF can also be solved for in the same fashion as in [9]. However, the parametric model is chosen to speed the computations since the benefits of the simultaneous model comprise the primary scope of the paper.

Example 1. The first example we consider is a clean vertical black bar with a gray region in the middle imposed on a white background as seen in Fig. 5(a). The inpainting domain will cover this gray region in the blurred image. This example was specifically chosen so that during the convolution, the information from the gray area will propagate into the non-occluded regions of the image. Hence, though not observable from the blurred image, there is more information available to the simultaneous method. Our model can utilize some of this information from the missing region since it is propagated to the non-occluded regions during the formation of the observed image (c.f. model (1)). The recovered images are shown in Fig. 5(e) for the non-blind deconvolution case and Fig. 5(f) for the blind deconvolution case. The results are very close to the original data in both cases with a clean reconstruction and little artifacts. In fact, there is little discernible difference between the recovered image from blind deconvolution and the one recovered from the non-blind deconvolution.

In Fig. 6(a) we have the result of inpainting the blurred-occluded image observed in Fig. 5(d). Here, we see that the result is very different from that of the blurred image in Fig. 5(c) (non-occluded region). This is mostly due to the fact that inpainting algorithms do not utilize the underlying process of the image formation. The errors resulting from this improper inpainting propagate into the deblurring step and in Fig. 6(b), ringing effects are observed. Moreover, the contrast of the restored image in the inpainting domain differs from the original clean image in Fig. 5(a).

Fig. 6(c) illustrates the deblurring of the occluded image in Fig. 5(d). Here, the improper boundary information in the inpainting domain propagates errors into the non-occluded regions of the image

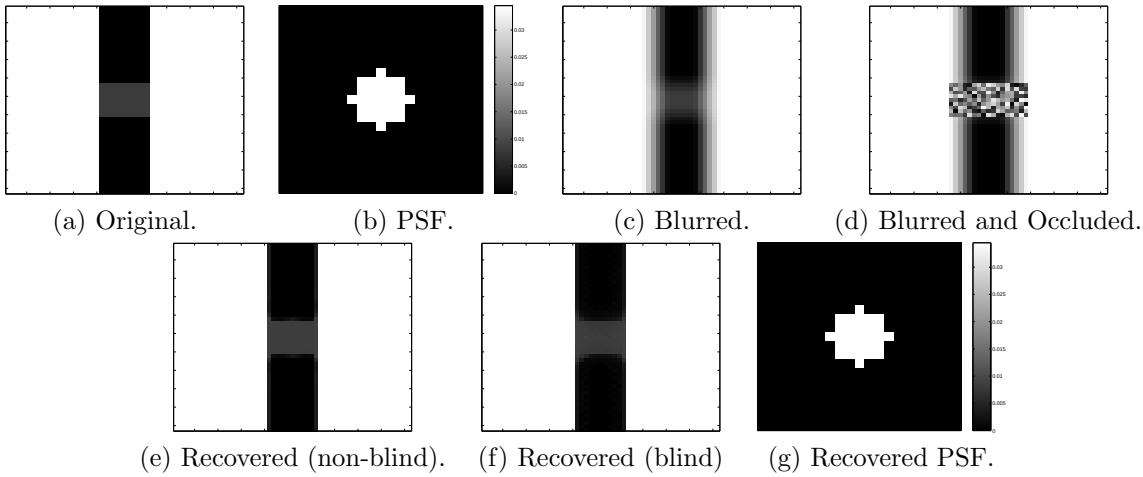

(a) Original. (b) PSF. (c) Blurred. (d) Blurred and Occluded.

(e) Recovered (non-blind). (f) Recovered (blind) (g) Recovered PSF.

Figure 5: Recovery of a missing gray region using the joint model (5).

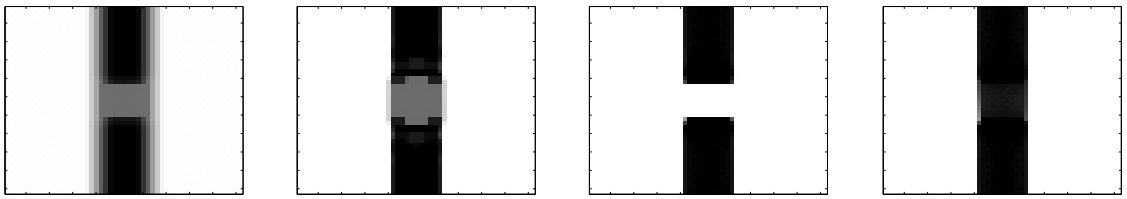

(a) Inpaint. (b) Inpaint then deblur. (c) Deblur. (d) Deblur then inpaint.

Figure 6: Separation methods for the recovery of Fig. 5(d).

during the deblurring. In the subsequent inpainting step, the errors from the previous deblurring propagate into the inpainting domain yielding an improperly inpainted image as seen in Fig. 6(d). This is particulary noticeable near the boundary of the inpainting domain. Moreover, the missing region in the original image is gray where the restored image in Fig. 6(d) has this region inpainted black.

We remark that in Fig. 6, the PSF is assumed to be known during the deconvolution step so that the ringing effects and restoration errors are truly due to the decoupling of the inpainting and deconvolution tasks. Furthermore, the results from the simultaneous model (5), even in the blind case, are significantly better than the decoupled methods in the non-blind case.

Example 2. The next example we consider is a blurred real image with scratches shown in Fig. 7(a). Due to the high degree of degradation to this image, the person is not identifiable? In Fig. 7(b) we have the restored image and the person is clearly recognizable.

We note that in Fig. 7(c), some of the scratches on the shirt are not completed while some others are. This is a well-known phenomenon with the TV inpainting model where the model chooses to connect the strips if the length of the gap is less than the width of the gap and chooses not to connect otherwise [7, 6]. If the completion of the strips on the shirt is desired, one may replace the TV inpainting method with some higher order inpainting methods such as curvature driven diffusion or Euler's elastica [5]; this is, however, beyond the scope of this paper.

(a) (b) (c)

Figure 7: SOS, who scratched the person! (a) Blurred and scratched image. (b) Recovered image from simultaneous inpainting-blind deconvolution. (c) Zoom-in of the left chest.

Example 3. In this example, we consider the blind restoration of a real image of a snake shown in Fig. 8(a). The blurred and scratched image is observed in Fig. 8(b) with the scratches shown in white. The image in Fig. 8(b) appears to be so severely degraded that the blurred object is no longer discernible.

The restored image from deblurring then inpainting is shown in Fig. 8(c). Here, there are visible ringing effects and artifacts in the reconstructed image. The white circles in 8(f) indicate some of the most noticeable ringing effects and artifacts of the restored image in Fig. 8(c). In 8(f), the two largest circles show some prominent ringing in the dark bands of the snake. The smallest circle points out an artifact in the background.

The restored image from inpainting then deblurring is shown in Fig. 8(d). Here, as in the deblurring then inpainting case, there are visible ringing effects in the reconstructed image. Some of the most prominent ringing effects are circled in white in Fig. 8(g). The two larger circles indicate the ringing effects in the dark bands of the snake while the smallest circle indicates ringing in the white band.

The restored image from the simultaneous method is shown in Fig. 8(e). The reconstructed snake is clearly visible and there are no observable ringing effects and very minimal artifacts. This example shows that for restoring images that have been significantly degraded, the simultaneous method is far superior to the separate methods making its use almost mandatory.

Example 4. In this example, we employ a synthetic image to illustrate the use of our model to generate boundary conditions for regular deconvolution problems. Fig. 9(a) and (b) show the original and the blurred images respectively. We compare the inpainting boundary conditions to the Neumann boundary conditions [4, 21]. To focus on the effects of the boundary conditions, we consider the non-blind deconvolution case where the PSF is known. In this way, the effects due to the errors in the recovery of the PSF are eliminated.

In the case of Neumann boundary conditions, we employ the model (3) with $\alpha = 10^i$ for $i = -1, 0, 1$ where the use of an α value outside the range $[10^{-1}, 10^1]$ only leads to poorer results. The deblurred results are shown in Fig. 9(c)–(e) respectively. Severe ringing effects are observed.

In Fig. 9(f)–(h), reconstructed images using the inpainting boundary conditions from the simultaneous model (5) with $\alpha = 10^1$, 10^0 and 10^{-1} are shown respectively. The restored images are significantly better. The corresponding relative errors (with respect to the original image) are shown in Fig. 9(i).

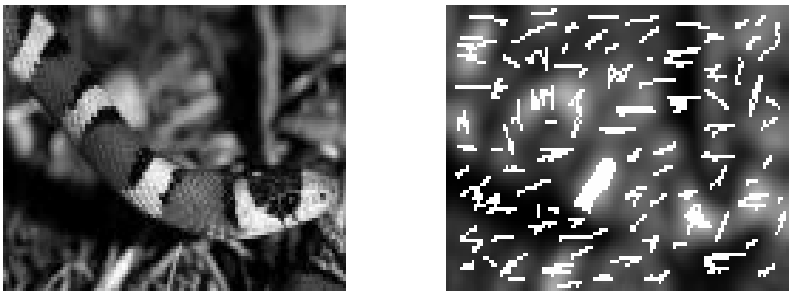

(a) Original image. (b) Degraded image (scratches in white).

(c) Deblur then inpaint. (d) Inpaint then deblur. (e) Simultaneous.

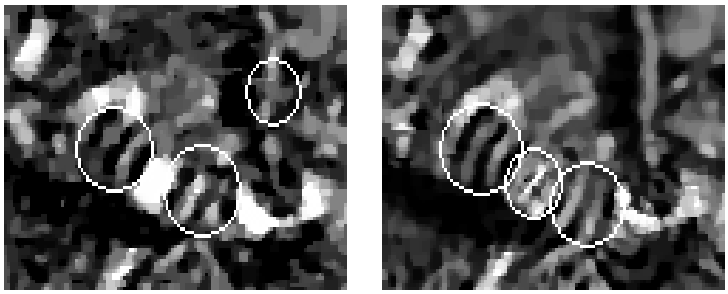

(f) Ringing effects from (c). (g) Ringing effects from (d).

Figure 8: (a) Original clean snake image. (b) Blurred and scratched image. The missing regions are shown in white (c) Recovered image from blind deconvolution then inpainting. (d) Recovered image from inpainting then blind deconvolution (e) Recovered image from simultaneous inpainting-blind deconvolution. (f) and (g) specify some prominent ringing effects and artifacts observed in (c) and (d) respectively.

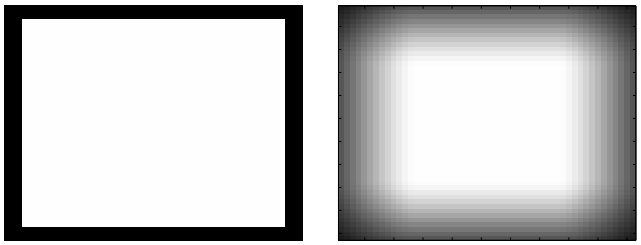

(a) Original. (b) Observed.

Neumann Boundary Conditions

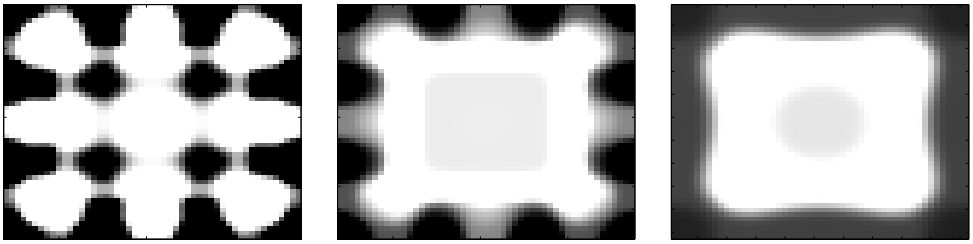

(c) $\alpha = 10^1$. (d) $\alpha = 10^0$. (e) $\alpha = 10^{-1}$.

Inpainting Boundary Conditions

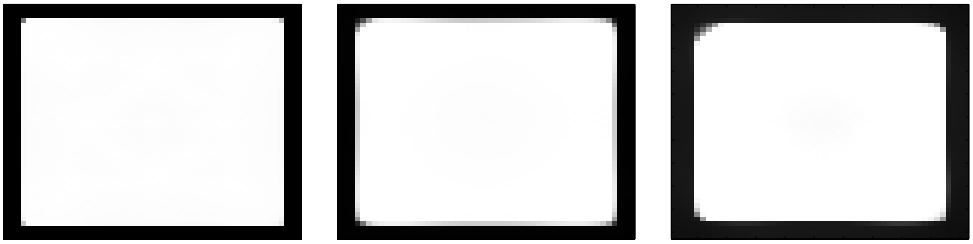

(f) $\alpha = 10^1$. (g) $\alpha = 10^0$. (h) $\alpha = 10^{-1}$.

α	10^1	10^0	10^{-1}
Inpainting B.C.	0.0144	0.0650	0.2715
Neumann B.C.	1.1050	0.3130	0.3105

(i) Relative errors of the recovered images.

Figure 9: Comparisons of the inpainting and Neumann boundary conditions using synthetic images.

Example 5. In this example, we compare the inpainting boundary conditions with the Neumann one using a real image and its blurred version shown in Fig. 10(a) and (b) respectively. Results (non-blind deconvolution) under the Neumann and inpainting boundary conditions are depicted in Fig. 10(c)–(e) and Fig. 10(f)–(h) respectively.

In the figures, ringing effects are clearly observed in all restored images, except for Fig. 10(h). This indicates the importance of imposing proper boundary conditions especially when the blurring is severe. However, as expected, the ringing effects are greatly reduced when inpainting boundary conditions are used. Moreover, the relative errors shown in Fig. 10(i) also reveal the superiority of the inpainting boundary conditions. We also observe that as α decreases, weighting applied to the TV regularization term in (5) increases, and hence the ringings are suppressed. But the detailed features of the images are lost at the same time. Overall, the result in Fig. 10(f) using inpainting boundary conditions with $\alpha = 10^3$ retains all the important features (the small letters) with acceptable amount of ringings and has the smallest relative error among the others.

There is another interesting observation from the results. The resulting ringing effects from the Neumann boundary conditions are horizontal stripes (c.f. Fig. 10(c)) while those from the inpainting boundary conditions are round shaped (c.f. black arrows in Fig. 10(d)). There seems to be two natural questions that arise: why the stripes are horizontal but not the other direction and why the ringings have different shapes across the two boundary conditions. We have not done any further experiments to give a full explanation to such a phenomenon yet. But we suspect that

- the ringing effects with the Neumann boundary conditions are horizontal lines simply because the left and right margins (almost constant background) in Fig 10(a) are wider than the top and bottom margins. Thus the reflected values along the left and right margins are closer to the true underlying boundary values than the reflected values along the top and bottom margins do. Hence, errors in the horizontal direction dominate the errors in the vertical direction. This fact is due to the nature of the image itself and similar effects are also observed in the results of the inpainting boundary conditions — the ripples in Fig 10(f) and (g) seem to come from several "sources" lying on the top and bottom boundaries;

- the ringing effects with the Neumann boundary conditions come from "sources" all along the top and bottom boundaries. Thus, by the Huygen's Principle, all the round shaped ripples/wavefronts (one from each "source") superimpose together to form horizontal stripes. In contrast to this, the inpainting boundary conditions only lead to a few "error sources" which are exactly located at the spots on the top and bottom boundaries where image gradient is relatively high. This may be another interpretation why the relative errors are smaller when the inpainting boundary conditions are used.

Example 6. The results of the inpainting boundary conditions in Example 5 are promising but it is still desirable to further eliminate the ringing effects to an unobservable extent while preserving the small scale features (the letters). To this end, we apply different amounts of TV regularization in the inpainted boundary and the original image domain:

$$\min_u E(u) \equiv \min_u \frac{\alpha}{2} \int_{D_o} (k * u - f)^2 dx + \int_{D_o} |\nabla u| dx + \lambda \int_{D_i} |\nabla u| dx.$$

The results are shown in Fig. 11. It can be seen that there are no ringing effects at all. Image features are also preserved in the same way as the results in Example 5. However, the price that we have to pay is the introduction of another parameter λ.

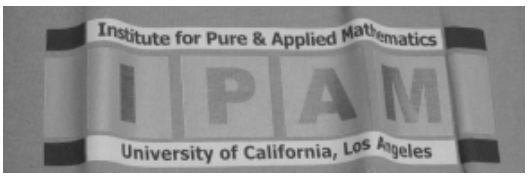

(a) Original.

(b) Observed.

Neumann Boundary Conditions

(c) $\alpha = 10^3$.

(d) $\alpha = 10^2$.

(e) $\alpha = 10^1$.

Inpainting Boundary Conditions

(f) $\alpha = 10^3$.

(g) $\alpha = 10^2$.

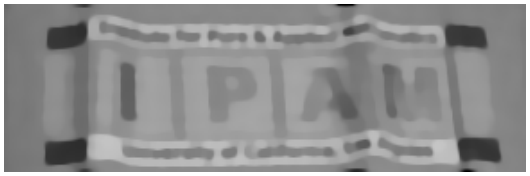

(h) $\alpha = 10^1$.

α	10^3	10^2	10^1
Inpainting B.C.	0.0798	0.0849	0.1000
Neumann B.C.	0.1380	0.0966	0.1037

(i) Relative errors of the recovered images.

Figure 10: Comparisons of the inpainting and Neumann boundary conditions using real images.

(a) $\alpha = 10^3$, $\lambda = 10^4$.

(b) $\alpha = 10^2$, $\lambda = 10^3$.

(c) $\alpha = 10^1$, $\lambda = 10^2$.

Figure 11: Recovered image using the inpainting boundary conditions and different amount of TV regularization on the boundary and the image domain.

7 Conclusion

In this paper, we introduce a model for simultaneous image inpainting and blind deconvolution which takes advantage of the coupling of the two problems near the interface of the inpainting domain and observed image domain. The experiments confirm that our method outperforms the decoupled methods. Moreover, our model can also be used for automatic boundary condition generation which produces more natural boundary conditions for image deconvolution problems resulting in significantly less ringing effects. Our model is also a very natural combination of the TV inpainting and TV blind deconvolution models that is easy to implement.

References

[1] M. Bertalmio, A. Bertozzi and G. Sapiro, Naview-Stokes, fluid-dynamics and image and video inpainting, IEEE CVPR 2001, Hawaii, USA, December 2001.

[2] M. Bertalmio, G. Sapiro, V. Caselles, and C. Ballester, Image Inpainting, Proc. of the 27th Annual Conference on Computer Graphics and Interactive Techniques (2000), pp. 417–424.

[3] M. Bertalmio, L. Vese, G. Sapiro and S. Osher, Simultaneous structure and texture image inpainting, IEEE Transactions on Image Processing 12:8 (2003), pp. 882–889.

[4] R.H. Chan, T.F. Chan, and C.K. Wong, Cosine transform based preconditioners for total variation deblurring, IEEE Transactions on Image Processing 8:10 (1999), pp. 1472–1478.

[5] T.F. Chan, S. Kang, and J. Shen, Euler's elastica and curvature-based image inpainting, SIAM J. Appl. Math. 63:2 (2002), pp. 564–592.

[6] T.F. Chan and J. Shen, Non-texture inpaintings by curvature-driven diffusions (CDD), J. Visual Comm. Image Rep. 12:4 (2001), pp. 436–449.

[7] T.F. Chan and J. Shen, Mathematical models for local nontexture inpaintings, SIAM J. Appl. Math. 62:3 (2002), pp. 1019–1043.

[8] T.F. Chan, J. Shen and L. Vese, Variational PDE models in image processing, Notices of the American Mathematical Society 50:1 (2003), pp. 14–26.

[9] T.F. Chan and C.K. Wong, Total variation blind deconvolution, IEEE Transactions on Image Processing 7:3 (1998), pp. 370–375.

[10] G. Golub, M. Heath and G. Wahba, Generalized cross-validation as a method for choosing a good ridge parameter, Technometrics 21 (1979), pp. 215–223.

[11] P.C. Hansen and D.P. O'Leary, The use of the L-curve in the regularization of discrete ill-posed problems, SIAM Journal on Scientific Computing 14 (1993), pp. 1487–1503.

[12] A.K. Katsaggelos and K.T. Lay, Simultaneous blur identification and image restoration using the EM algorithm, in Proc. SPIE Conf, Visual Communications and Image Processing IV 1199:3 (1989), pp. 1474–1485.

[13] D. Kundur and D. Hatzinakos, Blind image deconvolution, IEEE Signal Processing Magazine (1996), pp. 43–64.

[14] D. Kundur and D. Hatzinakos, A novel blind deconvolution scheme for image restoration using recursive filtering, IEEE Transactions on Signal Processing 46:2 (1998), pp. 375–390.

[15] R.L. Lagendijk and J. Bidmond, Iterative identification and restoration of images, Kluwer Academic Publishers, Massachusetts, USA, 1991.

[16] R.L. Lagendijk, A.M. Tekalp and J. Bidmond, Maximum likelihood image and blur identification: A unifying approach, Opt. Eng. 29 (1990), pp. 422–435.

[17] S. Lai and Y. Cui, Total variational blind image restoration from image sequences, Proc. SPIE Conf. Visual Communications and Image Processing, Kiyoharu Aizawa, Robert L. Stevenson, Ya-Qin Zhang, Eds., 3653 (1999), pp. 96–105.

[18] A. Likas and N.P. Galatsanos, A variational method for bayesian blind image deconvolution, Proc. of the Int. Conf. on Image Processing 2 (2003), pp. 973–976.

[19] S. Masnou and J.M. Morel, Level-lines based disocclusion, Proc. 5th IEEE Int. Conf. on Image Processing, Chicago, IL, USA 3 (1998), pp.259–263.

[20] V.A. Morozov, Methods for solving incorrectly posed problems, Springer, New York, USA, 1984.

[21] M.K. Ng, R.H. Chan, and W.C. Tang, A fast algorithm for deblurring models with Neumann boundary conditions, SIAM J. Sci. Comp. 21:3 (1999), pp. 851–866.

[22] M.K. Ng, R.H. Chan, T.F. Chan, and A.M. Yip, Cosine transform preconditioners for high resolution image reconstruction, Linear Algebra Appl. 316 (2000), pp. 89–104.

[23] M.K. Ng, R.J. Plemmons, and S. Qiao, Regularization of RIF blind image deconvolution, IEEE Transactions on Image Processing 9:6 (2000), pp. 1130–1134.

[24] C. Ong and J. Chambers, An enhanced NAS-RIF algorithm for blind image deconvolution, IEEE Transactions on Image Processing 8:7 (1999), pp. 988–992.

[25] S.I. Reeves and R.M. Mersereau, Blur identification by the method of generalized cross-validation, IEEE Transactions on Image Processing 1:3 (1992), pp. 301–311.

[26] L.I. Rudin, S. Osher, and E. Fatemi, Nonlinear total variation based noise removal algorithms, Physica D 60 (1992), pp. 259–268.

[27] S. Serra-Capizzano, A note on antireflective boundary conditions and fast deblurring models, SIAM J. Sci. Comp. 25:4 (2003), pp. 1307–1325.

[28] F. Šroubek and J. Flusser, Shift-invariant multichannel blind restoration, in Proc. Third Int. Symposium on Image and Signal Processing and Analysis 1 (2003), pp. 332–337.

[29] F. Šroubek and J. Flusser, Multichannel blind iterative image restoration, IEEE Transactions on Image Processing 12:9 (2003), pp. 1094–1106.

[30] C.R. Vogel and M.E. Oman, Iterative methods for total variation denoising, SIAM Journal on Scientific Computing 17 (1996), pp. 227–238.

[31] Y. You and M. Kaveh, A regularization approach to joint blur identification and image restoration, IEEE Transactions on Image Processing 5:3 (1996), pp. 416–427.

[32] Y. You and M. Kaveh, Blind image restoration by anisotropic regularization, IEEE Transactions on Image Processing 8:3 (1999), pp. 396–407.